Electronic Supplementary Material (ESI) for Physical Chemistry Chemical Physics.
This journal is © the Owner Societies 2018

Supplementary information

for

On the influence of multiple cations on the in-gap states and phototransport properties of iodide-based Halide Perovskites

Doron Azulay†[1,2], Igal Levine†[3], Satyajit Gupta[3], Einav Barak-Kulbak[3], Achintya Bera[3],Granit San[1], Shir Simha[2], David Cahen[3], Oded Millo[1] , Gary Hodes[3*], and Isaac Balberg[1*]

1. *The Racah Institute of Physics, The Hebrew University, Jerusalem 91904, Israel*
2. *Azrieli, Jerusalem college of Engineering, Jerusalem 9103501, Israel*
3. *Dept. of Materials & Interfaces, Weizmann Institute. of Science, Rehovot 76100, Israel*

† The authors contributed equally to this work

I. Solutions of the single level SRH model

In this part, we demonstrate the effect of shallow vs. deep recombination centers on the phototransport properties of the photoconductors studied, by using the single level Shockley-Read-Hall (SRH) model. We note here that the use of a single effective recombination level is well justified as long as the light intensity exponent[1] and the μτ(T) dependence are monotonic, whether this is, or is not, the actual electronic structure of the material. In fact from the photovoltaic point of view what counts are the observed μτ(T) dependence and not the recombination kinetics and transport that lead to its values[2]. Then, the simplest physical picture that accounts for these values is clearly the one that is preferable in enabling the observer to capture the basics of the recombination kinetics and transport of the system.

In our calculation we use the procedure that we have applied before[3]. We stress that although the material parameters used in the simulations may differ slightly from the exact properties of the MAPI and MCHP films studied here, the important parameters, relevant for this study, are E_c-E_r (or E_r-E_v) for the shallow level case, and E_r-E_F for the deep level case (as defined in the main text). Furthermore, in the two cases which were considered in the simulations, *only* these parameters are changed, to illustrate the effect of shallow vs. deep recombination centers on the phototransport properties. We further note that the specific position of E_F (as long as it is deep, i,e, E_c-E_F > E_F-E_v >> 12 kT), do not affect the results. The results of the model are obtained by simultaneously solving the kinetic equations for the holes and electrons [4–6]:

$$G = C_h p n_r - C_h p_1 p_r \qquad \text{(S1)}$$

$$G = C_e n p_r - C_e n_1 n_r \qquad \text{(S2)}$$

and the charge neutrality requirement:

$$(p-p_0)-(n-n_0) = (n_r-n_{r0}) \qquad \text{(S3)}$$

Here

- G is the electron and hole generation rate,
- C_h and C_e are the capture coefficients of holes and electrons by the recombination centers,
- p and n are the concentrations of holes in the valence and electrons in the conduction bands, resp. n_r is the concentration of the electron-occupied centers
- $p_r = N_r$-n_r is the concentration of the hole occupied centers p_r where
    - N_r is the total concentration of the recombination centers at the level E_r.

The subscript ”$_0$” in equations S2 and S3 indicates the equilibrium (dark) concentration of the corresponding quantity (e.g., $n_{r0} = N_r f(E_r)$ where $f(E_r)$ is the Fermi-Dirac electron occupation function) and $p_{r0} = N_r – n_{r0}$.

Also,

- $p_1 = N_v \exp[-(E_r-E_v)/kT]$, and
- $n_1 = N_c \exp[-(E_c-E_r)/kT]$, where
    - N_v is the effective density of states at the valence band edge, E_v, and
    - N_c is the effective density of states at the conduction band edge, E_c.
- n_0 and p_0 are then the equilibrium concentration of the electrons and holes in the dark which will be assumed below to be negligible compared to n and p.

We further use the common definitions of the corresponding carriers' lifetimes (or the trapping time by (or recombination time with) the opposite charge carrier in the recombination level) of the holes and the electrons as[4,7]:

$$\tau_h = p/G \qquad \text{(S4)}$$

and

$$\tau_e = n/G. \qquad (S5)$$

In the numerical solutions, we have solved the parameters n, p, and n_r, by providing reasonable parameter values for all other parameters in these equations (shown below and in Figures S1 and S2). We have described the numerical analysis used here in ref.[8] following the procedure of ref.[9].

Before turning to our calculations, we note two issues:

First, in our considerations of the kinetics we ignore the relatively small bimolecular process (as it appears to contribute little to the G values that are relevant to the phototransport regime that we consider here[4,10]).

Second, since in real materials the model of Fig. 2.1 can serve only as an *effective* presentation of a much more complicated electronic structure of levels in the band gap[11], it is expected to provide only semi-quantitative effective information regarding the behavior of the phototransport properties of the real system that is under study. However, such predicted behavior will be enough for the conclusions that we derive in Sec. IV of the main text. The great advantage of the simple model is that it can provide understanding of some basic trends in the phototransport behavior and, thus, enables us to interpret corresponding features in the experimental data[11–13] merely by using the minimal known values of the parameters included in equations S1-S3.

We note in passing that while mathematically the equations that describe the recombination process in this system, as given above, are simple and well-known[4,5,12], the corresponding analytic solution is very lengthy[6,11]. Thus, the analytic solutions can be derived, but they are non-transparent in the sense that without the reduction of many parameters, as can be done only in extreme cases[7], and/or the use of a graphic visualization of the solution[11], it is quite impossible to evaluate the effect of a particular parameter. This is the case for the effect of N_r, C_h, C_e, E_r and E_F, as well as for external-controllable parameters such as the temperature (T) and the carrier generation rate G[13], on the actual behavior of the photoconductivity, $\sigma_{ph}(G,T)$[4] and the ambipolar diffusion length, $L_D(G,T)$[14,1] (see below). The usual way to understand the basic physics of the phototransport processes is to apply the *a priori* known information (say, the position of E_F) and/or to consider extreme cases (say, very low or very high G for a given N_r)[4,7].

Correspondingly, in trying to understand the observed experimental results in detail one needs to compare these results with the graphically plotted results of the numerical solution[3,11–13]. Below we will assume constant values (independent of T and G) for the carrier mobilities and capture coefficients, in order to focus our attention on the recombination kinetics that are relevant to our conclusions regarding the MAPI and the MCHP films that we study.

Turning to the parameters used in the solution, we note that as there are many parameters in the model. To make the model more amenable for comparison with experimental results, we would like to narrow down the possible reliable microscopic scenarios that can account for the given experimental data[12]. In the present case (see Sec. IV) we know from theoretical calculations[15–17], experimental results of others[18–20] and our present STS data, that the band gap of the materials of interest is ~1.6 eV, and that when they are not intentionally doped, E_F lies deep in the band gap and the material is p-type[21–23]. From the present STS data and other studies[22,24], we could evaluate the corresponding position of E_F to be in the $0.4 \leq E_F\text{-}E_v \leq 0.6$ eV range for MAPI and MCHP. There were numerous reports on the mobility values in solution-processed halide perovskite films[25,26], from which mobility values that we use can be safely assumed to be in the $0.1 \leq \mu \leq 10$ cm^2/Vsec range, i.e. $\mu_e = 5$ cm^2/Vsec and $\mu_h = 0.25$ cm^2/Vsec. In fact, as we are concerned here with the kinetics, we will assume constant mobility values (independent of G and T) in our solutions of Eqs. S1-S3. Hence, the $\mu\tau$ solutions, to be presented below, reflect essentially only the temperature dependence of the lifetimes, τ.

The other reasonable parameters could be chosen based on accepted values that were derived in the literature. In particular, the capture coefficients C_e and C_h were reported to be in the 10^{-7}-10^{-9} cm^3/sec range[25,27] and the density of recombination centers, N_r, is generally accepted to be in the 10^{15}-10^{16} cm^{-3} range[19,24,25]. N_c and N_v values in MAPI are in the ~10^{18} cm^{-3} range[19,27]. As seen below, the exact values of these parameters are not critical for our conclusions and they are quite generally acceptable for the present materials and other semiconductors.

As for the parameters values used in the simulations, also listed in the legends of Figs. S1 and S2, the values used were: E_c-E_v = 1.6 eV. $C_e = C_h = 10^{-7}$ cm^3/sec, $N_r = 10^{15}$ cm^{-3}, $G = 10^{21}$ cm^{-3}sec^{-1} and $N_c = N_v = 2.4\text{x}10^{18}$ cm^{-3} (@ 300K). Hence, for the depth of E_r, which is the critical parameter that we will change, we took its value in the deep level case to be E_c-E_r = 0.8 eV (>>

12kT, noting that around this value the results are not too sensitive to the position of E_r) while for the shallow level case we took the value of E_c-E_r = 0.2 eV (≈ 7.5 kT). The latter value is consistent with some theoretical predictions[15–17], experimental results of others[28,29] and the direct STS result that we obtained in the present study on the MCHPs.

Before we turn to our numerical solutions of the SRH equations we will briefly consider the simple physics that one would expect for the temperature dependence of the phototransport properties with change of the energy E_r. In particular, let us consider the two cases, one where E_r is deep and another one when E_r is shallow with respect to the conduction band edge. We start with an intuitive physical picture and then turn to the visual exhibition of the solution of the SRH equation with the above-mentioned values for the microscopic parameters.

If E_r is well-removed (many kTs) from the band edges, E_c and E_v, but E_r is close to E_F, the level E_r, at $T \rightarrow 0$, will be occupied only by holes. As the temperature increases, the electron population will increase at the expense of the initial (i.e. T = 0) density of the N_r holes. Thus, at very high temperatures (above 300 K, therefore irrelevant for our case), the equilibrium population of both holes and electrons will approach $N_r/2$ for a given G. Correspondingly, the lifetime of the electrons will increase more rapidly at high temperatures and, even then, at most by a factor of 2. Therefore, over the temperature-range studied here (170-300K), this will only amount to a negligible increase. In contrast, for the holes, the density of the effective recombination centers for the capture of holes, n_r, will increase from 0 to $N_r/2$, i.e., $\mu_h\tau_h$ will decrease by orders of magnitude with even a relatively small increase of temperature. In practice however, in the temperature range of interest in our case, 167K-300K, the change in $\mu_h\tau_h$ is also negligible (a significant increase of $\mu_h\tau_h$ is expected to occur at $T > 350K$). These simple expectations are confirmed by the results of our SRH solutions that are shown in Fig. S1.

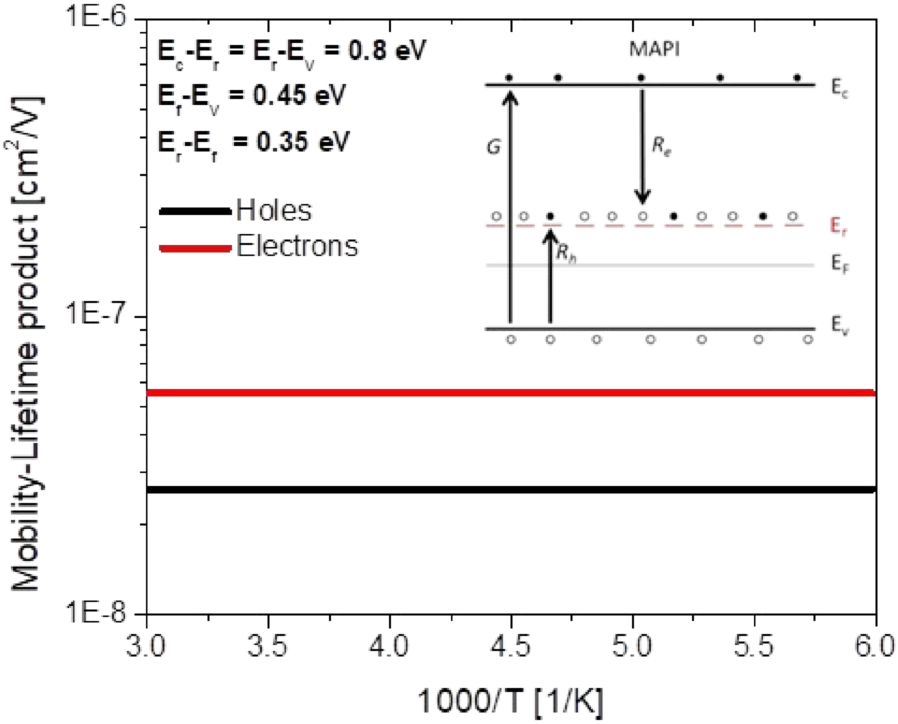

Fig, S1. Temperature dependence of $\mu\tau$ for a p-type semiconductor in which the recombination level is deep (i.e., E_r-E_V >> 12kT). The parameters used to derive these solutions, are given in the figure.

Turning to the shallow level case, we expect that in contrast to the above case, there will be now an increase of the two $\mu\tau$ products with increasing temperature. This increase follows the thermal excitation rate of the electrons that occupy states in E_r, to E_c, as manifested by the $g_e(T) = C_e n_1 n_r$ term in Eq. S2 and the $g_e(T)$ arrow in Fig. S2. In parallel, this decrease with temperature of n_r, (due to the thermal excitation of the electrons) will increase the hole lifetime.

The results of the solution, calculated with the same parameters that were used for Fig. S1, but now with a shallow (rather than a deep) position of E_r, are shown in Fig. S2. These results confirm the above-suggested physical scenario and clearly indicate that the increase of the $\mu\tau$ products with temperature is a signature of a shallow E_r. This result is in marked qualitative contrast with the relatively constant $\mu_h\tau_h$ product that was shown in Fig. S1 in the studied temperature range, which, as we saw above, is the signature of a deep lying E_r. The important point for the present study is that this different qualitative temperature dependence can indicate whether E_r is a deep or shallow recombination level. In practice, the change from T-decreasing (or nearly T independent) $\mu\tau$ products (Fig. S1) to T-increasing $\mu\tau$ products (Fig. S2), indicates the difference in the temperature dependence in the cases of a deep and a shallow level. In passing we remark that the temperature-dependent trends will be the same if the shallow recombination level is adjacent to E_v; the difference will be in the assignment (holes or electrons) of the $\mu\tau$ of the opposite carrier.

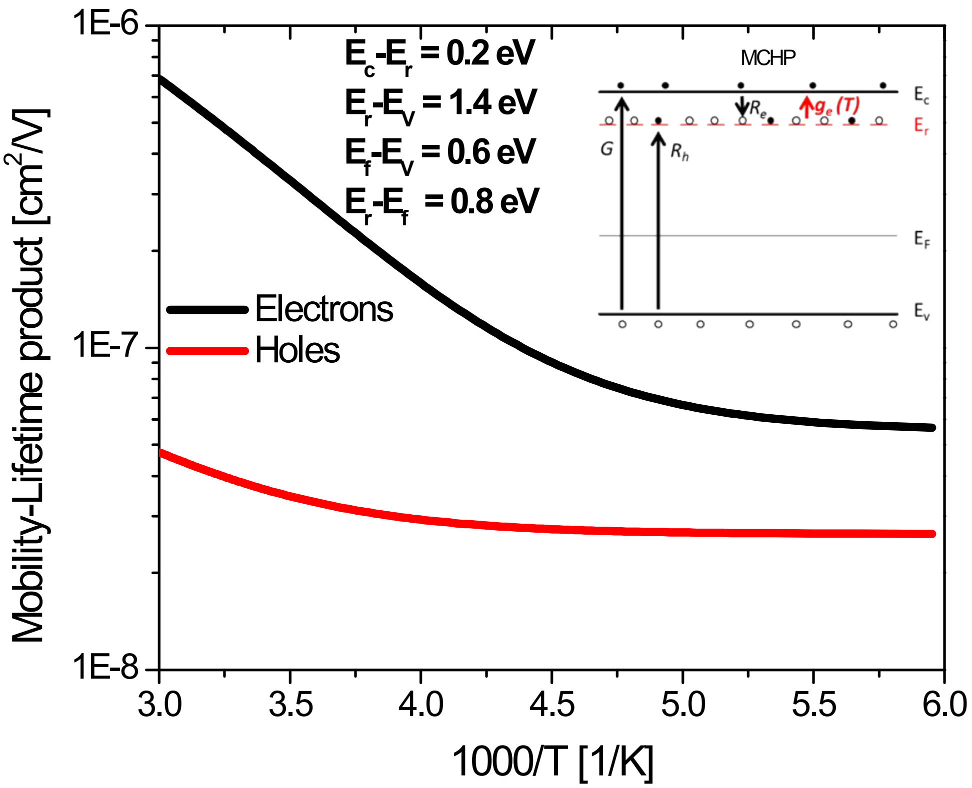

Fig. S2. Temperature dependence of $\mu\tau$ of a p-type semiconductor where the recombination level is close to the conduction band edge (E_c-$E_r \leq 12kT$, see legend). Note the increase of the $\mu\tau$ products of both types of carriers with increasing temperature. The parameters used here were the same as in Fig. S1, except that the position of the recombination level E_r is 0.2 eV (~ 7.5 kT @ RT, 300 K) below E_c compared to 0.8 eV (mid-gap) in Fig. S1.

In summary, as can be appreciated from Eqs. S1 and S2, the difference between the results of Figs. S1 and S2 is due to the $g_e(T)$ (i.e., $C_e n_1 n_r$) term in Eq. S2 that is negligible in the deep level case. While the more detailed physics of that will be discussed elsewhere, for the purpose of this study, the differences exhibited in the behaviors shown in the two figures is enough to make the connection between this indirect determination of the level position and the STS results. In other words, the increase with temperature of both $\mu\tau$ products with temperature is a convincing indication that recombination in the system takes place via a shallow recombination level. This is of course important in light of the states, revealed by the STS measurements, which can now be considered as those responsible for the phototransport behavior.

II. Experimental Details

Sample preparation

Single cation MAPI films were prepared by following a previously reported method[30]. In short, ~40 wt% of the perovskite precursor solution was prepared by dissolving MAI and $Pb(Acetate)_2{:}3H_2O$ (Sigma Aldrich) in anhydrous DMF in a 3:1 molar ratio. Then, 4.5 μL of hypophosphorous acid (HPA) solution was added to the DMF solution containing the precursors. The solution was spin-coated on the substrates in one step (2000 rpm for 40 sec) inside a glove box. After spin-coating the samples were annealed at 100°C for 5 minutes inside the glove box. The typical thickness of the MAPI film was around 300 nm.

Mixed cation MAPI, $FA_{0.79}MA_{0.16}Cs_{0.05}Pb(I_{0.83}Br_{0.17})_3$ (MCHP) films were fabricated as described elsewhere[31]. In short, the precursor solution was prepared in the following stoichiometric ratios: FAI [1 M] (Dyesol), PbI_2 [1.1 M] (Sigma Aldrich), MABr [0.2 M] (Dyesol), and $PbBr_2$ [0.22 M] (Sigma Aldrich) in anhydrous DMF:DMSO 4:1 (v:v) (anhydrous, Sigma Aldrich); CsI (Dyesol), (predissolved as a 1.5 M stock solution) was added to the MA+FA solution in a 5:95 molar ratio.

The triple cation solution was spin-coated in an N_2-filled glove box using a two-step program (1000 rpm for 10 sec, 4500 rpm for 20 sec). During the second step, 500 μL of chlorobenzene (anhydrous, Sigma Aldrich) was poured onto the substrate 10 sec prior to the end. The substrates were then annealed at 100 ºC for 1 hour inside the glove box. The typical thickness of the films was also around 300 nm.

Electrical contacts for transport measurements: For the STS measurements, 100 nm thick gold contacts were deposited on pre-cleaned microscope slides with a pre-deposited 10 nm Cr adhesion layer, using an E-beam evaporator, under 5x10^{-6} mbar base pressure, at a rate of 2Å/sec. The contact configuration for the PCS, PC and SSPG measurements was as described previously[32] with a 0.4 mm gap between the two electrodes.

Optical absorption was determined by measuring transmission and reflection of the thin films on glass using a Jasco V-570 spectrometer equipped with an integrating sphere. Transmission was corrected for reflection by $T_{corr} = T/(1-R)$, The absorbance is derived from the optical transmission measurements by A= 2-log (T%).

The photoluminescence spectra were excited at 640 nm with a picosecond pulsed diode laser (Picoquant LDH-P-C-640B). The energy of the pulse was ~5 × 10^{10} photons/cm^2 and the pulse duration was ~ 2-5 ns. The PL emission spectra and the PL decay characteristics were recorded using a photomultiplier tube (PMT Hamamatsu model H10721-01).

Photocurrent spectroscopy (PCS) measurements were done using a standard lock-in amplifier technique and the results (raw data) were normalized to the impinging photon flux. The measurements were taken in ambient and in vacuum (~ 10^{-5} mbar) conditions in an optical-cryostat as described in[33]. We note that these were measurements of photoconductivity (i.e. symmetrical contact configuration) and not photovoltaic currents (i.e. full cell configuration).

Scanning tunneling spectroscopy (STS) measurements

Local *I-V* characteristics were measured between the STM tip and the back electrode, at different locations on the sample surface[34,35]. During the measurements, the STM feedback loop was disconnected for a short period of time and the tunneling current was acquired with a constant tip-sample separation. The energy gap and features related to the local density of states, such as the band gap and the position of the Fermi level, were then deduced from the dI/dV-V spectra.

Atomic force microscopy: The topography of the studied sample was determined by topographic and friction scans of an atomic force microscope[34].

Steady-state photocurrents were measured as function of temperature and light intensity (i.e., carrier generation rate) in an optical cryostat[33]. The photo-excitation was generated by using a red laser, at 658 nm, with a maximum intensity of 0.04 W/cm^2. We estimate[24] the maximum generation rate to be (depending on the experimental set up) between $3.2\cdot10^{21}$ and 1.2 10^{22}

$(\mathrm{cm}^3\cdot\mathrm{s})^{-1}$. From the photocurrents (the dark current was negligible) we derived the photoconductivity σ_{ph}.

<u>*Ambipolar diffusion lengths*</u> were obtained from steady-state photocarrier grating, SSPG, measurements[36,37] using a HeNe laser with λ = 632 nm, 10 mW intensity, with a beam diameter[2] of 3 mm. In the SSPG method, described in more detail in[14,36,37]; two coherent light beams from the same laser, one of a much (20 x) higher intensity than the other, are made to coincide on the sample. Their coincidence is made to be coherent or incoherent by changing the light polarization of the more intense beam. Experimentally one determines the parameter β which is the ratio between the decrease of the photocurrent (with respect to the photocurrent induced by only the higher intensity beam), when the photograting is *present* (the coherent beams case) and the increase of the photocurrent (with respect to the photocurrent induced by only the higher intensity beam) when the grating is *absent* (the incoherent beam case). The β parameter is related to L_D, the ambipolar diffusion length, via the "Balberg plot" relation[37,38]:

$$\sqrt{\frac{2}{1-\beta}} = \frac{1}{\sqrt{\gamma {\gamma_0}^2}} \left(\frac{1}{\Lambda^2}\right) (2\pi L_D)^2 + \frac{1}{\sqrt{\gamma {\gamma_0}^2}} \tag{S6}$$

where γ is the power law exponent of the photoconductivity γ_0 is the grating quality factor, which is usually taken close to 1, Λ is the period of the grating, and L_D is the ambipolar diffusion length[24,39]. Thus, by plotting the left-hand term of Eq. S6 vs. $\frac{1}{\Lambda^2}$, L_D is obtained from the linear fit according to:

$$L_D = \frac{1}{2\pi} \sqrt{\frac{slope}{intercept}} \tag{S7}$$

Having σ_{ph} and L_D we then derived the above-mentioned mobility-lifetime products from the experimental measurements of the photoconductivity σ_{ph} [4,9] and the ambipolar diffusion length L_D [1,24] (see Sec. III), by simply solving the well-known relations between these measurable quantities and the microscopic $\mu\tau$ properties[24,36,37,39]:

$$\sigma_{ph} = q(\mu_e\tau_e+\mu_h\tau_h)G, \tag{S8}$$

and

$$L_D = [(2kT/q)(\mu_e\tau_e\mu_h\tau_h)/(\mu_e\tau_e+\mu_h\tau_h)]^{1/2}, \qquad \text{(S9)}$$

where q is the electronic charge, kT is the thermal energy, μ_e(μ_h) is the electron (hole) mobility and τ_e (τ_h) is the electron (hole) recombination (or trapping) time. In our work, the above two equations were solved for some values of the controllable parameters G and T. The results of this analysis are shown in Figs (3.6) and (3,7). The error in the values of the mobility-lifetime products was calculated based on the experimental error in the determination of L_D. The error for the L_D values was calculated according to the resulting error in the intercept and slope of the linear fit of Eq. S7, for every temperature. In passing we note here that because of the symmetry of the two μτs in the two equations, one can only distinguish between majority and minority carriers. To identify which one is associated with the electrons and which one is associated with the holes, one has to know a priori which carrier is the majority one. As mentioned above this information is derived from independent theoretical or experimental considerations. In our case of the MAPI and the MCHP, we assumed throughout that the majority carriers in the dark and under illumination are the holes following our measurements, the theoretical consideration and the overwhelming evidence in the literature on solution-processed films[25].

III. Comparison of the PCS and optical absorption results

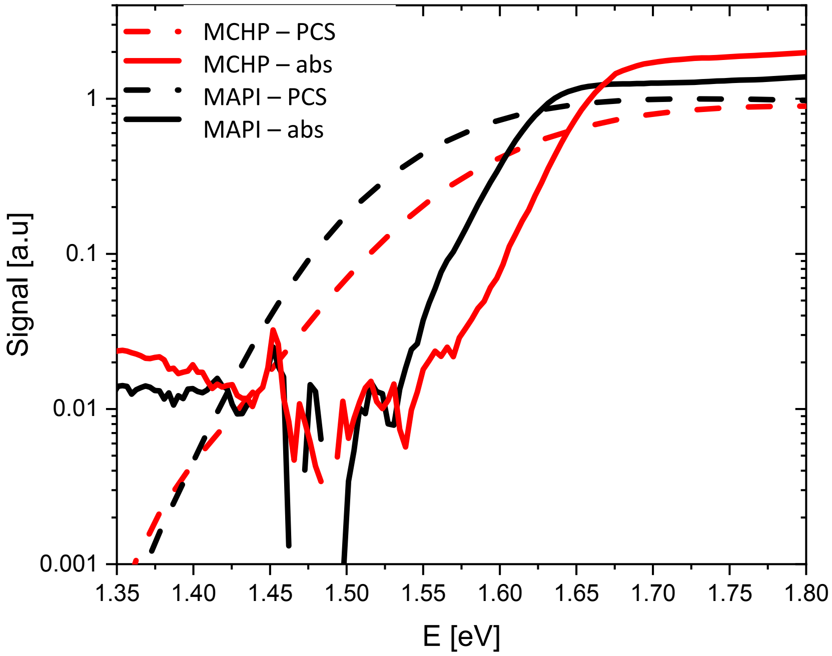

Fig. S3. Semi-log plot of the PCS (dashed lines) vs. the optical absorption results (full lines) for MAPI (black) and mixed MCHP films (red).

Table S1: *Comparison between the extracted band gaps of the MAPI and MCHP samples from the various methods used in this study (for the PCS method, where near gap states are likely to contribute, the real bandgap may be higher, apart from the given experimental errors)).*

	Optical absorption	PL	PCS	STS
MAPI	1.60	1.60	1.47	1.53
MCHP	1.64	1.62	1.52	1.50

**The error in the optical absorption, PL and PCS methods is ~0.02eV, while for the STS the error is ~0,.05-0.10eV.*

We note that although the STS-derived bandgap should in principle be larger than the optical bandgap by the e-h binding energy, the binding energy in our case is less than 20 meV, which is much smaller than the experimental error in the STS bandgap measurements, and hence we ignore it here.

References

(1) Balberg, I. The Theory of the Photoconductance under the Presence of a Small Photocarrier Grating. *J. Appl. Phys.* **1990**, *67* (10), 6329–6333.

(2) Misiakos, K.; Lindholm, F. A. Analytical and Numerical Modeling of Amorphous Silicon *P* - *I* - *N* Solar Cells. *J. Appl. Phys.* **1988**, *64* (1), 383–393.

(3) Balberg, I.; Naides, R.; San, G. Temperature Dependence of the Phototransport Properties in C 60 Films. *Fuller. Sci. Technol.* **1998**, *6* (1), 39–57.

(4) Bube, R. H. *Photoelectronic Properties of Semiconductors*; Cambridge University Press, 1992.

(5) Sze, S. M.; Ng, K. K. *Physics of Semiconductor Devices*; Wiley-Interscience: Hoboken, 2007.

(6) Blakemore, J. S. *Semiconductor Statistics*; Dover Publications, 1987.

(7) Rose, A. *Concepts in Photoconductivity and Allied Problems*; Interscience, New York, 1963.

(8) Balberg, I.; Naidis, R. Sensitization of the Minority-Carrier Lifetime in a Photoconductor. *Phys. Rev. B* **1998**, *57* (12), R6783–R6786.

(9) Vaillant, F.; Jousse, D. Recombination at Dangling Bonds and Steady-State Photoconductivity in *a* -Si:H. *Phys. Rev. B* **1986**, *34* (6), 4088–4098.

(10) Song, D.; Cui, P.; Wang, T.; Wei, D.; Li, M.; Cao, F.; Yue, X.; Fu, P.; Li, Y.; He, Y.; et al. Managing Carrier Lifetime and Doping Property of Lead Halide Perovskite by Postannealing Processes for Highly Efficient Perovskite Solar Cells. *J. Phys. Chem. C* **2015**, *119* (40), 22812–22819.

(11) Balberg, I.; Dover, Y.; Savir, E.; von Huth, P. Basic Physics of Phototransport as Manifested in Thin Films of In-Doped CdTe. *Phys. Rev. B* **2010**, *82* (20), 205302.

(12) Lubianiker, Y.; Biton, G.; Balberg, I.; Walter, T.; Schock, H. W.; Resto, O.; Weisz, S. Z. Dependence of the Phototransport Properties on the Position of the Fermi Level in Polycrystalline CuInS2 Films. *J. Appl. Phys.* **1996**, *79* (2), 876.

(13) Balberg, I.; Dover, Y.; Naides, R.; Conde, J. P.; Chu, V. State Distribution in Hydrogenated Microcrystalline Silicon. *Phys. Rev. B* **2004**, *69* (3), 35203.

(14) Orton, J. W. (John W.; Blood, P. (Peter). *The Electrical Characterization of Semiconductors : Measurement of Minority Carrier Properties*; Academic Press, 1990.

(15) Shi, H.; Du, M.-H. Shallow Halogen Vacancies in Halide Optoelectronic Materials. *Phys. Rev. B* **2014**, *90* (17), 174103.

(16) Kim, J.; Lee, S.-H.; Chung, C.-H.; Hong, K.-H. Systematic Analysis of the Unique Band Gap Modulation of Mixed Halide Perovskites. *Phys. Chem. Chem. Phys.* **2016**, *18* (6), 4423–4428.

(17) Yin, W.-J.; Shi, T.; Yan, Y. Unusual Defect Physics in CH3NH3PbI3 Perovskite Solar Cell Absorber. *Appl. Phys. Lett.* **2014**, *104* (6), 63903.

(18) Tahara, H.; Endo, M.; Wakamiya, A.; Kanemitsu, Y. Experimental Evidence of Localized Shallow States in Orthorhombic Phase of $CH_3NH_3PbI_3$ Perovskite Thin Films Revealed by Photocurrent Beat Spectroscopy. *J. Phys. Chem. C* **2016**, *120* (10), 5347–5352.

(19) Herz, L. M. Charge-Carrier Dynamics in Organic-Inorganic Metal Halide Perovskites. *Annu. Rev. Phys. Chem.* **2016**, *67* (1), 65–89.

(20) Brenner, T. M.; Egger, D. A.; Kronik, L.; Hodes, G.; Cahen, D.; Weller, M. T.; Weber, O. J.; Henry, P. F.; Pumpo, A. M. Di; Hansen, T. C.; et al. Hybrid Organic—inorganic Perovskites: Low-Cost Semiconductors with Intriguing Charge-Transport Properties. *Nat. Rev. Mater.* **2016**, *1* (1), 15007.

(21) Hutter, E. M.; Hofman, J.-J.; Petrus, M. L.; Moes, M.; Abellón, R. D.; Docampo, P.; Savenije, T. J. Charge Transfer from Methylammonium Lead Iodide Perovskite to Organic Transport Materials: Efficiencies, Transfer Rates, and Interfacial Recombination. *Adv. Energy Mater.* **2017**, 1602349.

(22) Zohar, A.; Levine, I.; Gupta, S.; Davidson, O.; Azulay, D.; Millo, O.; Balberg, I.; Hodes, G.; Cahen, D. What Is the Mechanism of MAPbI $_3$ P-Doping by I $_2$? Insights from Optoelectronic Properties. *ACS Energy Lett.* **2017**, *2* (10), 2408–2414.

(23) Senocrate, A.; Moudrakovski, I.; Kim, G. Y.; Yang, T.-Y.; Gregori, G.; Gr?tzel, M.; Maier, J. The Nature of Ion Conduction in Methylammonium Lead Iodide: A Multimethod Approach. *Angew. Chemie Int. Ed.* **2017**.

(24) Levine, I.; Gupta, S.; Brenner, T. M.; Azulay, D.; Millo, O.; Hodes, G.; Cahen, D.; Balberg, I. Mobility–Lifetime Products in MAPbI3 Films. *J. Phys. Chem. Lett.* **2016**, *7* (24), 5219–5226.

(25) Hutter, E. M.; Eperon, G. E.; Stranks, S. D.; Savenije, T. J. Charge Carriers in Planar and Meso-Structured Organic–Inorganic Perovskites: Mobilities, Lifetimes, and Concentrations of Trap States. *J. Phys. Chem. Lett.* **2015**, *6* (15), 3082–3090.

(26) Chen, Y.; Yi, H. T.; Wu, X.; Haroldson, R.; Gartstein, Y. N.; Rodionov, Y. I.; Tikhonov, K. S.; Zakhidov, A.; Zhu, X.-Y.; Podzorov, V. Extended Carrier Lifetimes and Diffusion in Hybrid Perovskites Revealed by Hall Effect and Photoconductivity Measurements. *Nat. Commun.* **2016**, *7*, 12253.

(27) Sherkar, T. S.; Momblona, C.; Gil-Escrig, L.; Ávila, J.; Sessolo, M.; Bolink, H. J.; Koster, L. J. A. Recombination in Perovskite Solar Cells: Significance of Grain Boundaries, Interface Traps, and Defect Ions. *ACS Energy Lett.* **2017**, *2* (5), 1214–1222.

(28) Duan, H.-S.; Zhou, H.; Chen, Q.; Sun, P.; Luo, S.; Song, T.-B.; Bob, B.; Yang, Y. The Identification and Characterization of Defect States in Hybrid Organic–inorganic Perovskite Photovoltaics. *Phys. Chem. Chem. Phys.* **2015**, *17* (1), 112–116.

(29) Rosenberg, J. W.; Legodi, M. J.; Rakita, Y.; Cahen, D.; Diale, M. Laplace Current Deep Level Transient Spectroscopy Measurements of Defect States in Methylammonium Lead Bromide Single Crystals. *J. Appl. Phys.* **2017**, *122* (14), 145701.

(30) Zhang, W.; Saliba, M.; Moore, D. T.; Pathak, S. K.; Hörantner, M. T.; Stergiopoulos, T.; Stranks, S. D.; Eperon, G. E.; Alexander-Webber, J. A.; Abate, A.; et al. Ultrasmooth Organic–inorganic Perovskite Thin-Film Formation and Crystallization for Efficient Planar Heterojunction Solar Cells. *Nat. Commun.* **2015**, *6*, 6142.

(31) Saliba, M.; Matsui, T.; Seo, J.-Y.; Domanski, K.; Correa-Baena, J.-P.; Nazeeruddin, M. K.; Zakeeruddin, S. M.; Tress, W.; Abate, A.; Hagfeldt, A.; et al. Cesium-Containing

Triple Cation Perovskite Solar Cells: Improved Stability, Reproducibility and High Efficiency. *Energy Environ. Sci.* **2016**, *9* (6), 1989–1997.

(32) Balberg, I.; Lubianiker, Y. Evidence for the Defect-Pool Model from Induced Recombination Level Shifts in Undoped *a* -Si:H. *Phys. Rev. B* **1993**, *48* (12), 8709–8714.

(33) Wolf, O.; Millo, O.; Balberg, I. Phototransport Spectroscopy of Ensembles of Si Quantum Dots. *J. Appl. Phys.* **2013**, *113* (14), 144314.

(34) Azulay, D.; Balberg, I.; Chu, V.; Conde, J. P.; Millo, O. Current Routes in Hydrogenated Microcrystalline Silicon. *Phys. Rev. B* **2005**, *71* (11), 113304.

(35) Azulay, D.; Balberg, I.; Millo, O. Microscopic Evidence for the Modification of the Electronic Structure at Grain Boundaries of Cu (In 1 − X , Ga X) Se 2 Films. *Phys. Rev. Lett.* **2012**, *108* (7), 76603.

(36) Ritter, D.; Zeldov, E.; Weiser, K. Steady-State Photocarrier Grating Technique for Diffusion Length Measurement in Photoconductive Insulators. *Appl. Phys. Lett.* **1986**, *49* (13), 791.

(37) Balberg, I.; Delahoy, A. E.; Weakliem, H. A. Self-Consistency and Self-Sufficiency of the Photocarrier Grating Technique. *Appl. Phys. Lett.* **1988**, *53* (11), 992.

(38) Goerlitzer, M.; Beck, N.; Torres, P.; Meier, J.; Wyrsch, N.; Shah, A. Ambipolar Diffusion Length and Photoconductivity Measurements on “‘midgap’” Hydrogenated Microcrystalline Silicon. *J. Appl. Phys.* **1996**, *80* (9), 5111.

(39) Yang, L.; Catalano, A.; Arya, R. R.; Balberg, I. Effect of Low-Level Boron Doping and Its Implication to the Nature of Gap States in Hydrogenated Amorphous Silicon. *Appl. Phys. Lett.* **1990**, *57* (9), 908.